Metallic impurity content behavior during ICRH in EAST

G. Urbanczyk[a,b,c,d], L. Colas[d], X.J. Zhang[c], R. Dumont[d], W. Tierens[e], E. Lerche[f],
D. Van Eester[f], S. Heuraux[g], A. Ekedahl[d], C.M. Qin[c], Y.P. Zhao[c], X.D. Yang[c], L. Zhang[c],
J.C. Xu[c], Y. Peysson[d], A. Grosjean[d], N. Fedorczak[d], J.G. Li[c]

[a] *Advanced Energy Research Center, Shenzhen University, Shenzhen 518060, China*
[b] *Key Laboratory of Optoelectronic Devices and Systems of Ministry of Education and Guangdong Province,*
College of Optoelectronic Engineering, Shenzhen University, Shenzhen 518060, China
[c] *Institute of Plasma Physics, Chinese Academy of Sciences, Hefei 230031, People's Republic of China*
[d] *CEA, IRFM, F-13108 Saint Paul-Lez-Durance, France.*
[e] *Max-Planck-Institut für Plasmaphysik, Boltzmannstrasse 2,D-85748 Garching, Germany*
[f] *Laboratorium voor Plasmafysica - Laboratoire de Physique des Plasmas, Association 'EURATOM -*
Belgian State', Trilateral Euregio Cluster, 30 Avenue de la Renaissance, B-1000, Brussels, Belgium
[g] *IJL, UMR 7198, CNRS-U. de Lorraine, F-54506 Vandoeuvre Cedex, France*

guiguiurban@hotmail.com

Abstract.

High-Z impurity production is often observed during Ion Cyclotron Range of Frequencies (ICRF) wave injection. This can be the consequence of several co-existing physical processes; near and far fields induced RF sheaths on top of natural thermal sheath. This study uses the diversity of materials in the Experimental Advanced Superconducting Tokamak (EAST) to extract, via Extreme UV (EUV) spectrometry in the plasma core, local information on which plasma-surface interaction process is dominant during Ion Cyclotron Resonance Heating (ICRH). Intensities of EUV spectral lines characteristic of each material, normalized to line-integrated plasma density, exhibit different parametric dependencies over scans of ICRH and LH (Lower Hybrid) power and for different toroidal phasing between straps, strap power balance and magnetic configurations. This diversity of behavior is interpreted as the signature of different physical processes. Before 2017 only the upper divertor region contained tungsten (W). Large increase in core W content could be observed when moving from lower (LSN) to upper single null (USN) configurations. The W content was then found to better correlate with the total injected power than the ICRH power, despite signs of RF-induced SOL biasing recorded locally by arrays of triple probes embedded on divertors away from the strike points. Mo, covering the part of the inner wall facing one ICRF antenna (I-port), was mainly sensitive to the ICRH power from this antenna, as well as to the phasing of its straps. Modelling suggests a possible interaction of the inner wall with residual ICRF waves crossing the plasma. Materials close and magnetically-connected to an active antenna show better correlation with ICRF antenna electrical tuning than those which are far away or not connected. This is in particular the case of W since 2018, when the limiter tiles of the LH launchers were changed from graphite into tungsten. In these latter conditions, it is finally shown that, W sources at the mid-plane (equatorial plane) contribute to a significant fraction of the core contamination by tungsten (25% in ohmic regime and more during ICRH).

1. Introduction.

In view of future experiments on larger devices like ITER and the China Fusion Engineering Test Reactor (CFETR), the Experimental Advanced Superconducting Tokamak (EAST) aims at long pulses at high power in steady state. Higher power demand nevertheless comes with challenges in terms of plasma surface interaction and impurity mitigation. Methods for optimizing high power scenarios using more of the 12MW ICRH power available at the generator depend a priori on where the impurities are produced, and on which physical mechanisms play a role in their production. This study focuses on impurity production issues

in discharges with ICRH in EAST, and their dependency on their spatial origin in the vacuum chamber. Different magnetic configurations are also explored to analyze in more details the contribution of different divertor areas.

ICRH wave coupling can be quite poor in EAST [1]. On top of thermal sheath present on any PFC intercepting a magnetic flux tube, high RF near-fields are also excited leading to DC potential rectification, which is known for enhancing plasma-wall interactions. This can have particularly deleterious effects near antennas where the strongest near-fields occur. To a smaller extent this can remain true further away, and sometimes even in non-magnetically connected regions due to far-field interactions [2] as observed on many devices like Tore Supra [3] [4], Alcator C-Mod [5] [6] [7], JET [8], ASDEX Upgrade [9] and LAPD [10]. The ICRH wave absorption efficiency – estimated by comparing the break-in-slope technique with the ITER89-P scaling law in ref. [11] – was found to be generally low (~35%). In this case, a significant part of unabsorbed power might well lead to far-field-induced interactions in unexpected locations, hence the need to localize and characterize impurity sources at least qualitatively [12, 13, 14]. One difficulty in this study comes from the lack of appropriate edge diagnostics to characterize most impurities sources, like visible spectroscopy lines of sight pointing anywhere but to the upper divertor [8, 15], meaning that most high-Z impurities can, in EAST, only be seen in the core using an Extreme UltraViolet (EUV) spectrometer [16, 17]. The present study uses the diversity of materials in EAST to extract local information on localized plasma-surface interaction. This diversity of materials includes titanium in a location only magnetically connected to one ICRH antenna (B-port, magenta in Figure 1), and tungsten in the LH grill's four lateral limiters (since 2018, before they were graphite). Even if we mostly focus on the characterization of ICRH-related sources of impurities, a secondary objective is to identify dominant mechanisms in different regions. Comparisons between different campaigns and magnetic configurations were exploited to extract qualitative information on impurity sources.

We first introduce the experimental protocol before discussing the influence of magnetic connections, RF phasing, and power, on impurities presumably produced from different surfaces. Total injected power influence on both ICRF waves absorption and impurity release from divertor region are discussed in the last section. Comparing situations with and without tungsten at the mid-plane (equatorial plane), the last section shows that the main sources of impurities are located around the mid-plane in surfaces magnetically connected to ICRH antennas.
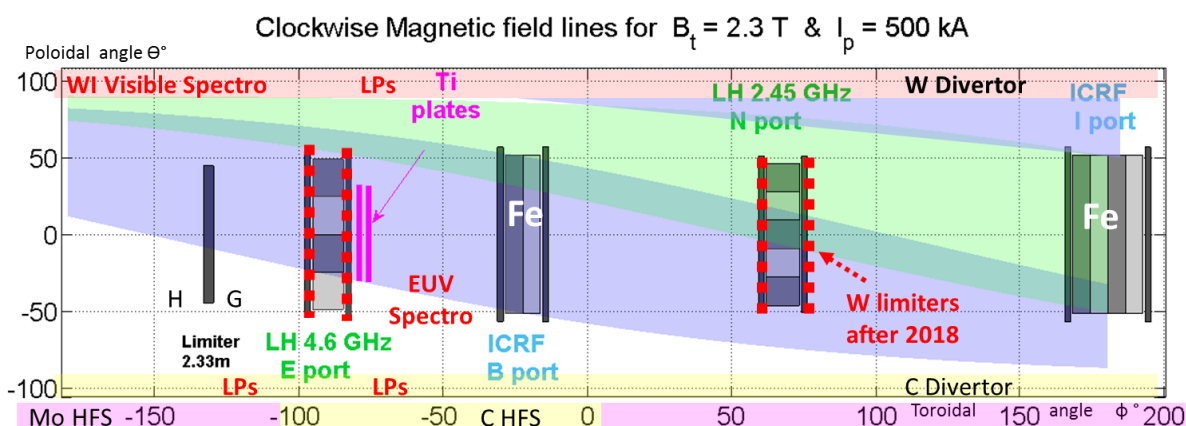

Figure 1. Toroidal-Poloidal (ɸ-Θ) 2D map of EAST showing magnetic connections between objects, materials, heating systems and EUV spectrometer, seen from center of the torus with one half of high field side wall in Mo and the other half in graphite.

2. Experimental conditions and protocol in EAST.

EAST is a superconducting tokamak equipped with two divertors allowing double null, lower (LSN) and upper single null (USN) configurations with the following parameters for this study: toroidal magnetic field B_t=2.3T, plasma current I_p=500kA, major radius R_o=1.85m, minor radius a=0.44m, triangularity δ=0.5 and elongation κ=1.65. Plasma isotopic ratio (H/H+D) rarely decreases below 5% in EAST. Lithium coating is therefore daily applied before each session (1 gram), mainly to keep low-Z impurities like oxygen and carbon down to acceptable levels in terms of radiated power. Lithium can also have mitigating effects on high-Z impurity contamination like tungsten [18]. This mitigation decreases during the experiments as Li is eroded and redeposited elsewhere. In this study all plasmas were in L-mode and USN configurations. Key auxiliary heating systems for our study are Lower Hybrid Current Drive (LHCD) and ICRH. EAST is also equipped of two neutral beam injectors and one 170GHz electron cyclotron Gaussian beam launcher that will only be used on some cases in the last section of this paper aiming that this additional heating acts only on the global transport. Lower Hybrid is almost always used for driving current and helps doing steady state discharges. The two launchers are located in the E-port (4.6 GHz and 1.79<$n_\parallel$< 2.26) and N-port (2.45 GHz and 1.85< $n_\parallel$ <2.6) [19]. Only in the last section will we present data obtained after the LH launchers' lateral protections were upgraded from graphite to tungsten. The two ICRH antennas are heating hydrogen minority in deuterium plasmas; one is located in the B-port (31.5 MHz) and composed of two arrays of two straps and the other is located in the I-port (35 MHz) and composed of an array of four straps (Figure 1) [1, 2, 20]. When not mentioned, all straps in a given antenna were fed with RF currents of comparable magnitude in dipole phasing (with 180° phase difference between RF-currents in toroidally-adjacent straps). It is important to mention that ICRH phases were not real-time controlled, which will be discussed in section 4.

Using a flat-field extreme ultraviolet (EUV) spectrometer [21], the brightness of various high-Z impurity lines (20Å to 150Å) were investigated. Spectra emitted by the plasma are reflected with 87° incidence on a concave holographic grating focal-plane and collected by a CCD camera of 26.6×6.6mm² with 1024×255 pixels. Wavelength resolution can be optimized down to 0.22-0.3Å defined as full width at half maximum. Lines brightness are systematically normalized by line-integrated plasma density, and their parametric variations from pulse to pulse within the same experimental session are interpreted as a change in the sources of impurities rather than their transport. This assumption is fairly good for most species which radiate relatively close to the edge and easily penetrate inside plasma. Note this can be questionable for W coming from the divertor region, as it is not only expected to be better screened but also its emissivity mainly comes from plasma center, and is therefore more sensitive to transport in both SOL and confined plasma. As far as edge turbulent transport is concerned, it has been shown in several devices that it usually does not change much in presence of ICRH [22, 23]. As for neoclassical transport, we acknowledge some changes may occur, yet as temperature and density profiles remained fairly similar along the experiments, this transport is not expected to significantly change our conclusions. More importantly, T_e in the core did not change much (<10% as shown in Figure 3f) and its profile remained relatively flat at the center without fast particles. The spectrometer was moreover measuring W continuum. These assumptions guarantee that W brightness measured by the EUV spectrometer was not significantly influenced by T_e changes. This assumption will anyways be benchmarked by neutral tungsten (WI) visible spectroscopy, with 16 lines of sight covering both the inner and the outer targets of the upper divertor at 150Hz sampling rate.

Ions	λ (Å)	$E_i \sim T_e$ (keV)	ρ
Ti^{17+}	144.76	1.2	< 0.7
Mo^{31+}	127.87	1.8	< 0.5
Fe^{22+}	132.91	1.9	< 0.6
W-UTA=$W^{24+\rightarrow45+}$	45→70	0.5	< 0.85
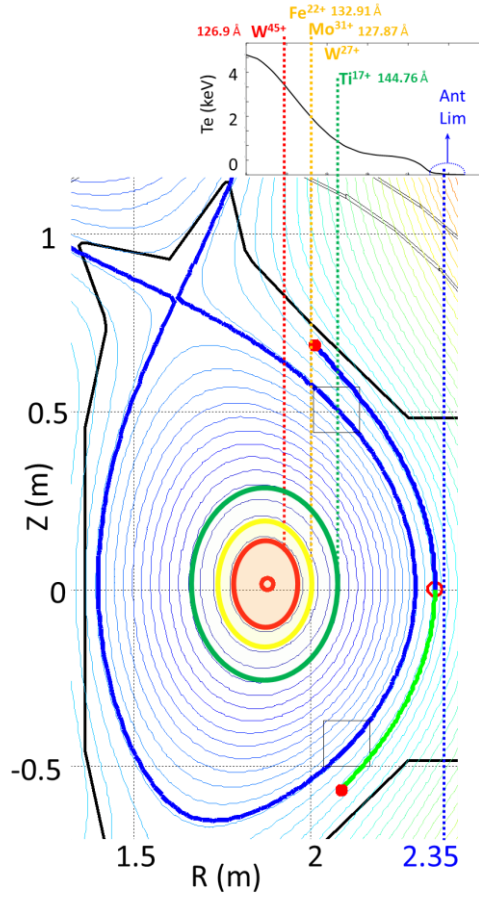
Figure 2. Spectral lines observed by EUV spectrometer in the present study with the corresponding emitted wavelength λ, minimal temperature T_e and normalized radius ρ at which ionization occur

Different lines, corresponding to the different materials summarized at the top of Figure 2 are seen as footprints of plasma-material interaction in a relatively precise location on the inner surface of the device; Iron is found on antenna Faraday screens (underneath a boron carbide coating), the upper divertor is made of tungsten (noted W for W_{UTA}, which is an average of all spectral lines from W^{27+} up to W^{45+}) and molybdenum (Mo) that covers half of the high field side wall ($-180° < \phi < 180°$ and $-90° < \Theta < 90°$ as indicated by pink regions on the bottom of Fig. 1). In addition, two titanium (Ti) passive plates were installed at one toroidal location of the outer mid-plane for the specific purpose of serving as impurity tracers ($\phi \sim -90°$ and $-30° < \Theta < 30°$). Ti was found appropriate mainly for three reasons; a spectral line can easily be distinguished with EUV spectrometer from those of others species present in EAST, it can be used as a permanent plasma facing component without affecting the vacuum conditions and its cost is reasonably low. Table 1 summarizes materials position in the tokamak.

The blue area in Figure 1 shows that only the B-port ICRH antenna magnetically connects to the Ti plates while only the I-port antenna faces the Mo inner wall tiles. Such location was chosen to confirm the role of magnetic connections in RF sheaths formation [24] and ICRH-enhanced plasma-surfaces interactions.

In the following, the different spectral lines are monitored over scans of ICRH and LH power by several combinations of both antennas, with several toroidal phasing between straps.

Materials	Location
C	Limiters and Lower divertor
Fe	ICRH antennas Faraday screens
Ti	Between D and E port Mag. Connected to B-port
Mo	All walls except 130° of the high field side facing B-port
W	**Before 2018** : Only upper divertor
	After 2018 : Upper divertor and LH launchers limiters

Table 1. Summary of materials location in EAST

3. Links between ICRH and impurities production

The objective of the following series of shots is to give an idea of how different species behave according to their position in EAST and their magnetic connections to with active ICRH antennas. A first typical shot only heated with 1.4MW LH power (black curves in Fig. 3) sets a reference level for each impurity without ICRH. Another shot (red curves) represents a case when the B- and I-port ICRH antennas were also powered successively in dipole phasing and with 5Hz modulations of power between 0.5 and 1MW as shown in graph e. Both shots' electron temperature and density were very similar and are represented on Figure 3f. The same graph shows the radiation power from bolometry which increases significantly with ICRH, while plasma energy content (Figure 3g) does not change much, suggesting either that ICRH power is not well coupled or not well absorbed. Typical L-mode steady D-alpha signal is also provided in Figure 3g.

All metal impurity signals increase fairly similarly during application of LH power, except Mo which appears particularly insensitive. It is worth mentioning that, seen from our EUV spectrometer [16], the Mo^{31+} line is hard to distinguish compared to other species, such that its temporal evolution is not always easy to interpret. When the ICRH antennas are activated, Ti and Fe contents in the plasma increase and correlate strongly with power modulations visible on both signals. As Fe and Ti-covered objects are both magnetically connected to the B-port antenna, the strongest interactions occurred when this antenna was active. Fe is also well connected to the I-port antenna, so we expect similar levels in both cases, but since the B-port antenna is much smaller, higher power densities are expected for same antenna loading and power. However, Mo showed opposite behavior and higher content was observed when the I-port antenna was powered. Since Mo is symmetrically present all around the vessel's low field side, we believe it does not come from there, otherwise it should follow a similar trend as Fe. As represented on Figure 1 by the pinkish region, the I-port faces Mo high field side wall whereas the B-port faces carbon. Impurities variations over an experimental phase scan of I-port antenna hints that Mo might come from the high field side wall facing the I-port. This will be presented in the next section together with modelling results supporting this claim. In the next subsection, we show that W originating from the divertor region seems to react equally to ICRH and LH power. We show that the RF rectification on divertor targets plays a minor role on impurity productions. Launched ICRH power can either be lost at the edge, or absorbed by the plasma and increase fluxes on divertor. A discussion on ICRF waves' absorption efficiency is therefore added and a correlation with total injected power is found. Finally, the last subsection discusses near-fields effects on surfaces magnetically connected to active antennas.
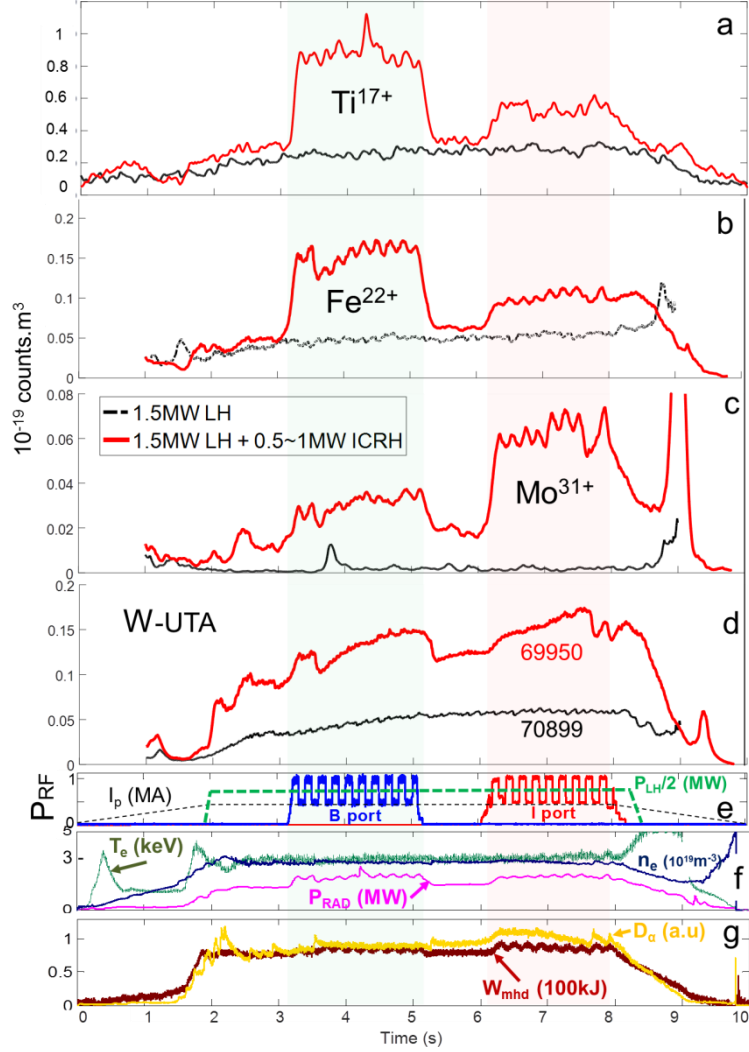
Figure 3. High-Z spectral lines brightness from EUV spectrometer normalized by line-integrated density of; titanium XVIII (a), iron XXIII (b), molybdenum XXXII (c), tungsten (d), ICRH, LH powers and plasma current (e), radiated power from bolometry, electrons temperature from ECE and density from interferometry (f), plasma energy (W_{mhd}) and $D\alpha$ (g), for EAST #70899 and ICRH heated #69950 pulses

From Figure 3, we know that the total ICRH power ($P_{ICRH} = P_I + P_B$) is not itself a fully relevant parameter to estimate impurity levels as power from I (P_I) and B ports (P_B) have different influence on different impurities. It consequently matters to have a relatively constant ratio P_I/P_B over power scan, which is kept close to unity ($P_I \approx P_B$). Since plasma shape did not change much, EUV spectral line intensities were systematically normalized to line-integrated density from interferometer and averaged over small periods of time (between 0.02 and 0.1s) and noted *Imp*. For each species and shot, ICRH-related impurity production Y_{shot} is calculated as:

$$Y_{shot} = (Imp_{withIC} - Imp_{withoutIC}) / \max(Imp_{withIC} - Imp_{withoutIC})_{over.all.shots} \qquad (1)$$

3.1 Far-field effects on inner wall

The high field side wall is a surface almost never magnetically connected to active ICRH antennas at the low field side. Interactions at the high field side are therefore in principle not correlated to what happens at the low field side as seen on Mo behavior in Fig. 3. A way ICRH may have an impact on the inner wall is through the far-field, often resulting from a poor absorption efficiency leading to residual ICRH power crossing the plasma. By changing the phase difference between RF currents on toroidally adjacent straps of an IRCH antenna, the

launched spectrum changes together with wave propagation and absorption properties. This allows discussing ICRH far-fields effects on the inner wall. In EAST, only phases of the I-port antenna were changed whereas the B-port antenna always operated in presumably dipole phasing. A series of shots with similar power and loadings on both antennas and different phases on the I-port antenna were studied and results shown in Figure 4. Ti, Fe and W remained relatively insensitive to the phase variation, which is surprising as both modelling (see appendix) and results from other devices respectively predict higher fields and an increase in impurity production as phasing tends towards monopole [1, 9, 25]. On the one hand the absence of real time feedback control of EAST ICRH port phasing [26] can be blamed, but on the other hand Mo content varied in agreement with what is expected from observations in other devices, namely an increase in Mo production going from dipole to monopole. Once again, this peculiar observation leads us to consider the high field side wall as a likely source of Mo correlated with the I-port antenna settings.
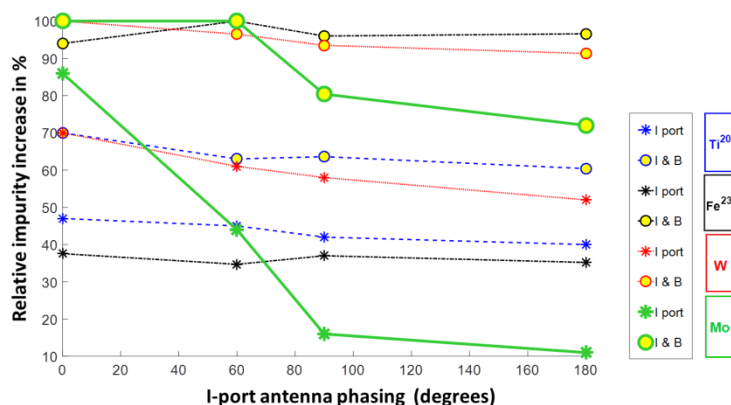

**Figure 4. ICRH-related impurity production increase (Y_{shot}) versus I-port antenna phases**

Note the B-port antenna still remains the principal cause of impurity production, which can be partially understood considering its size, twice smaller than the I-port antenna, leading to much higher power densities for similar generator power and loadings. This is particularly visible for the Fe characteristic of near-field interactions, whose level is quite low all over the I-port phase scan and increases by 150% when the B-port is activated.

Knowing this, and that Mo cover all low field side walls, if it were to come from the low field side, it would behave like Fe. Mo is however sensitive to I-port phasing, suggesting that it may come from the high field side wall facing I-port. Since dedicated experiments to answer on the origin of Mo are too challenging due to the lack of appropriate diagnostic, wave propagation and absorption were respectively simulated with EVE 3D [27] and TOMCAT 1D [28] codes. Both codes' results indeed point towards probable Mo source at the high field side. TOMCAT predicts a degradation of the single pass absorption from 50% in dipole phasing down to 15% in monopole phasing. On the real part of the iso-contours of the left-handed polarized electric field (Figure 5) mode conversion can also be seen at the center with increasing residual power reaching the inner wall as phasing decreases to zero. When this residual power is reflected on the inner wall, part of the fast wave mode can be converted into slow wave and excite RF sheath. Where RF sheath excitation and the resulting plasma surface interactions are concerned, the parallel component of the electric field ($E_∥$) is the most directly-related parameter to look at. Figure 6 shows the amplitude |$E_∥$| which dramatically increases at the high field side as phasing gets closer to monopole (ϕ =0°). These simulations suggest that as phasing shrinks to zero, absorption efficiency declines and mode conversion occurs. These fields on the inner wall are likely responsible for enhancing plasma surface interaction on the Mo surfaces at the high field side. So-called positive and negative field polarizations are also available in appendix 1 (Fig. A1) to better exhibit mode conversion nearby resonance layer (R=1.7m). It can also be seen on loaded spectra in Fig. A2b that less than 60° phasing leads to

the excitation of low $k_{//}$ modes which are poorly absorbed and can result in proper modes in the plasma. These modes propagate in plasma edge and can lead to power losses and further enhance plasma surface interactions.
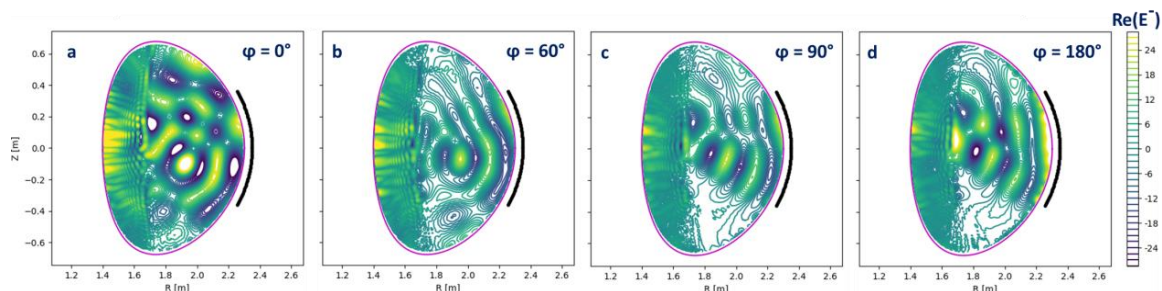
Figure 5. Iso-contours of the left-handed polarized electric field (real part), in kV/m, assuming 4.6MW of total absorbed RF power for various phasings of the I-port ICRH antenna
(a) φ=0°, (b) φ=60°,(c) φ=90°,(d) φ=180°
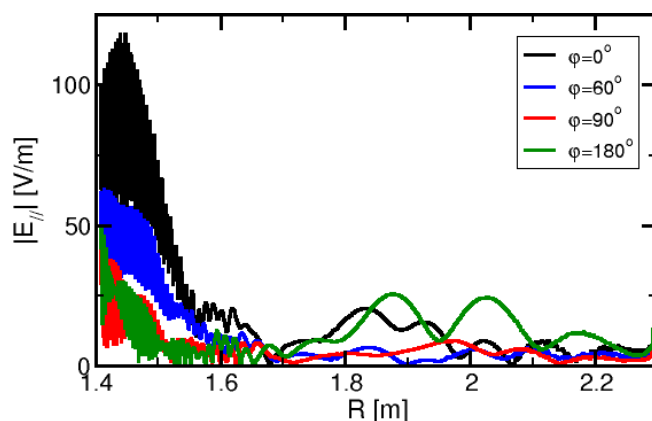
Figure 6. **Parallel component of the electric field (in V/m) in the equatorial plane, for the same conditions as in Fig. 5.**

We can also look how Mo behaves while changing ICRH power and keeping phasing as close as possible to dipole on both antennas. Three series of shots with scan of P_{ICRH} at generator in different conditions were analyzed. Y_{shot} as defined in eq. 1 is represented in Figure 7 for Mo. In the blue series only P_{ICRH} increased, while in the black series P_{ICRH} increased together with P_{LH}. In the red series, power balance on the B-port antenna straps is changed over the scan: one of the four radiating straps is typically switched off as the power is increased on the other straps. Through black and blue series in Figure 7, Mo seems to have no obvious correlation with the ICRH power. The red series confirms the negligible impact of B-port antenna on Mo, consistent with a source at the inner wall facing I-port.

Note decreasing phasing closer to zero not only has consequences on far-fields but also on near-fields as shown in appendix A2 and in Fig. 7 of [20]. Near-fields effects will be discussed in further details in section 3.3.
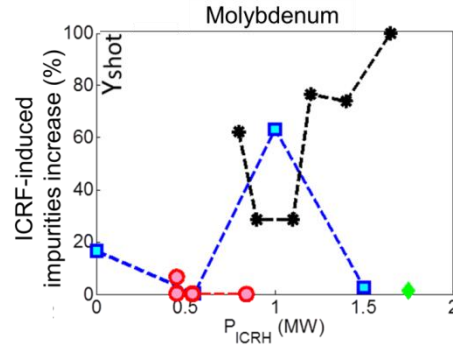
Figure 7. ICRH-related Mo production (Y_{shot}) as a function of ICRH power. In the blue series, LH power remained constant while it changed in the black series. Power balance on straps was changed in the red series. Green dot corresponds to a discharge only heated with ICRH power (balanced on all straps)

3.2 Divertor region, a combination of all effects

In this section will only be discussed cases before 2018, when W could only be found in the upper divertor. We will therefore interpret W continuum from the EUV spectrometer as a modification of W source assuming transport does not have a strong impact on core W content. Y_{shot} as defined in eq. 1 is represented in Figure 8a for W.

For constant ICRH power, we observe similar W content when the power is unbalanced (red series) than when it is well balanced (blue series). This suggests that the divertor region is insensitive to the antenna settings and only depends on the power injected. Furthermore, looking at the cases when ICRH increases together with LH power (black series), W content increases strongly hinting that the divertor region is sensitive to the total power injected rather than ICRH power alone. This can be confirmed by tracing impurity increase as function of P_{TOT} for all shots (Figure 8b). The impurity increase is defined as $|Imp_{during\ IC} - Imp_{before\ IC}|$ with ICRH (red series) otherwise $|Imp_{during\ LH} - Imp_{before\ LH}|$ (black series). Note the linear trend of both black and red dots, meaning that W production increases in similar fashion with LH and ICRH.
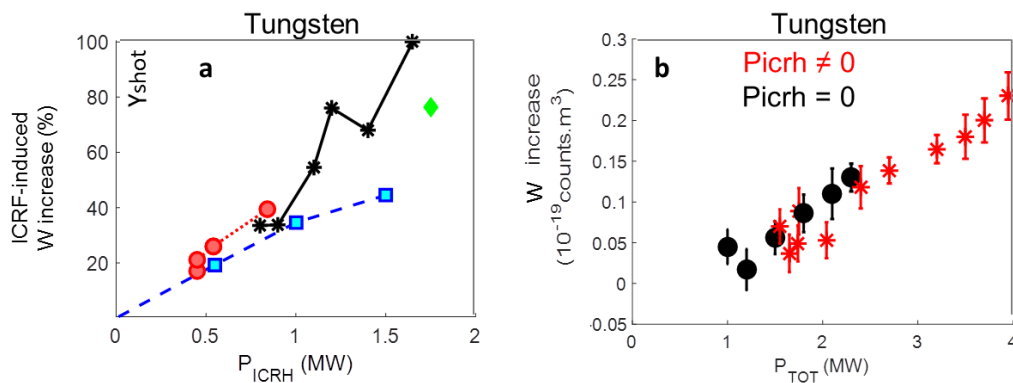
Figure 8. W production (Y_{shot}) as a function of (a) ICRH power and (b) total power. Blue, red and black series in graph a correspond to the same shots as in Figure 7. Graph b also represents to the same shots but points without ICRH (black series) were added as well.

Considering how linear the red and blue trends are in Figure 8a, we should now look after footprints of non-linear RF sheath through potential rectification in the divertor region. This is provided in Figure 9, representing floating potential and electron density profiles along upper divertor targets measured by Langmuir probes along the black series power scan. In the case without ICRH (black curve), potential and density rectifications are weak, but when ICRH is activated (colored curves) rectification is significantly stronger and increases together with

ICRH power. Along the power scan, the inner strike point shifted from a probe onto another, explaining differences in some inner probes signals. This stands as a footprint of the effect of ICRH in the divertor region, and its localization is furthermore consistent with another dedicated study [34]. However, we know from the red and blue series in Figure 8 that such rectification did not cause significant core W content increase.
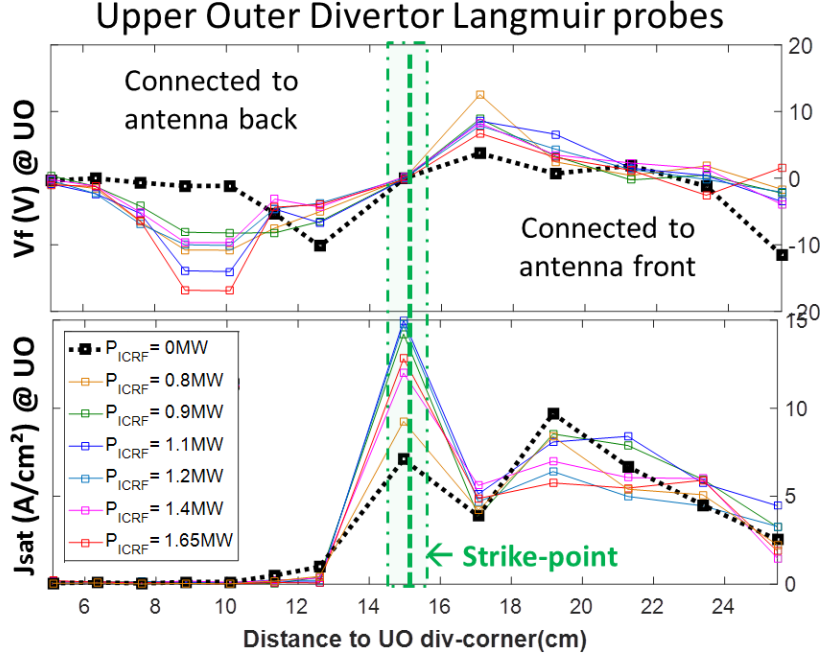
Figure 9. Floating potential V_f and ion saturation currents J_sat profiles from outer target of the upper divertor for different ICRH power

If we assume that the energy absorbed by the plasma ends up on the divertor targets, this can be interpreted in terms of difficulties either to couple waves to the plasma or to have them absorbed efficiently. Since coupling efficiency remained fairly stable along the experiment, observation made in the divertor region might show some correlation with ICRF absorption efficiency, estimated based on the break-in-slope method [29]. This method consists in fitting plasma energy W_{ENG} increase when applying ICRH by an exponential, providing the confinement time τ_e:

$$W_{ENG}(t) = W_{ENG}^{beforeICRF} - \left(W_{ENG}^{beforeICRF} - W_{ENG}^{afterICRF} \right)\left(1 - \exp(-t/\tau_e) \right) \qquad (2)$$

W_{ENG} is measured by diamagnetic probes and its variations are often slightly delayed compared to the ICRH power application, which was taken into account for each fit.
The absorption efficiency is finally calculated as follows:

$$\eta_{ICRH}^{Abs} = \left(\frac{\Delta W_{ENG}}{\tau_e} - \frac{\Delta V_{loop}}{I_p} + \Delta P_{RAD} \right) \bigg/ \left(\alpha P_{ICRH}^{in} - \frac{P_{ICRH}^{refl}}{\alpha} - \Delta P_{RAD} \right) \qquad (3)$$

With Δ meaning the difference between times with and without ICRH, and α the ratio of ICRH power lost in the transmission lines between the antennas and the voltage probes providing incident and reflected powers. The denominator basically represents the effective power step when applying ICRH. Beyond the fact that these estimations are based on single power steps – not optimal for absorption efficiency estimations – their main weakness comes from large uncertainties in power losses in transmission line, such that the coefficient α may vary between 50 and 90%. For our calculations in L-mode, we assume the most optimistic case of only 10% losses (α=0.9). We will not discuss quantitative results but rather look at qualitative trends. This exercise was made for each shot of the three series introduced in the previous section. Ratios of absorbed power against total power injected P_{TOT} were plotted as function of P_{TOT} in Figure 10. The result shows that ICRF wave absorption improves with total power injected. In the present regime of operation, since relatively little power is injected, ICRF

absorption efficiency is often poor compared to those of lower hybrid. In addition, larger power fraction is radiated during ICRH than during LH. As a conclusion, (i) the divertor target is mostly sensitive to the conducted power, and (ii) the power conducted by LH is often much higher than the one conducted by ICRH, therefore (iii) divertor region is well-correlated to total injected power (mostly LH) rather than ICRH. If the total injected power could be significantly increased, we would expect better ICRF absorption efficiency, more conducted power and therefore an increase of W production in the divertor region. Note for different heating conditions represented by each series in Figure 10, absorption does not seem to improve at the same rate, yet the lack of statistics does not allow drawing any strong conclusion.
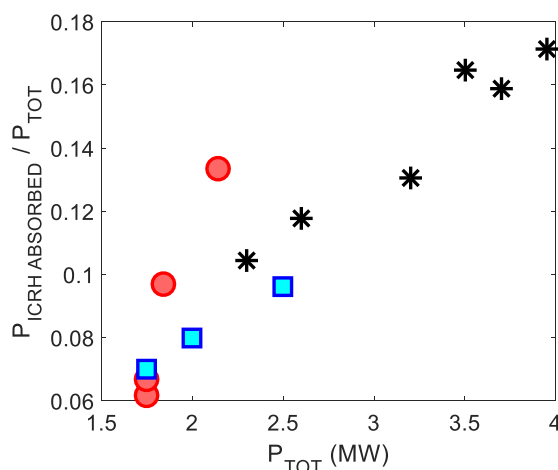

Figure 10. ICRF waves' absorption efficiency normalized by total power injected as a function of total power injected

To finally confirm that the divertor region is only sensitive to the amount of power injected regardless of how it may have been launched, we propose to compare rectified potential changes observed by divertor Langmuir probes [30] (Figure 11) and W sources from one visible spectroscopy line of sight (Figure 12) in both USN and LSN configurations. Figure 11 shows time evolutions of floating potential profiles along outer targets of both upper (W) and lower (C) divertors during a LSN discharge partially heated with ICRH. We see that ICRH-related potential rectification occurs in very similar fashion at the upper and lower targets. Furthermore noticing potential rectifications obtained at the lower divertor are comparable to those obtained at the upper divertor (Figure 11), RF rectification in divertor targets does not seem to depend on the magnetic configuration but rather on magnetic connections to antenna front face [34]. Based on this observation, if RF rectification played a key role in EAST divertors erosion, at least for ICRH dominated discharges, we would expect to get comparable erosion rates in both configurations. However, as shown by WI line brightness (neutral W visible spectroscopy) for two discharges in similar conditions but different configurations (Figure 12), upper divertor erosion rate is much higher in USN than LSN configuration.
As far as EAST and relatively low ICRH power are concerned, these observations allow concluding that RF rectification does not play a strong role in the erosion region of the divertor which is more sensitive to total conducted power and of course magnetic configuration [34].
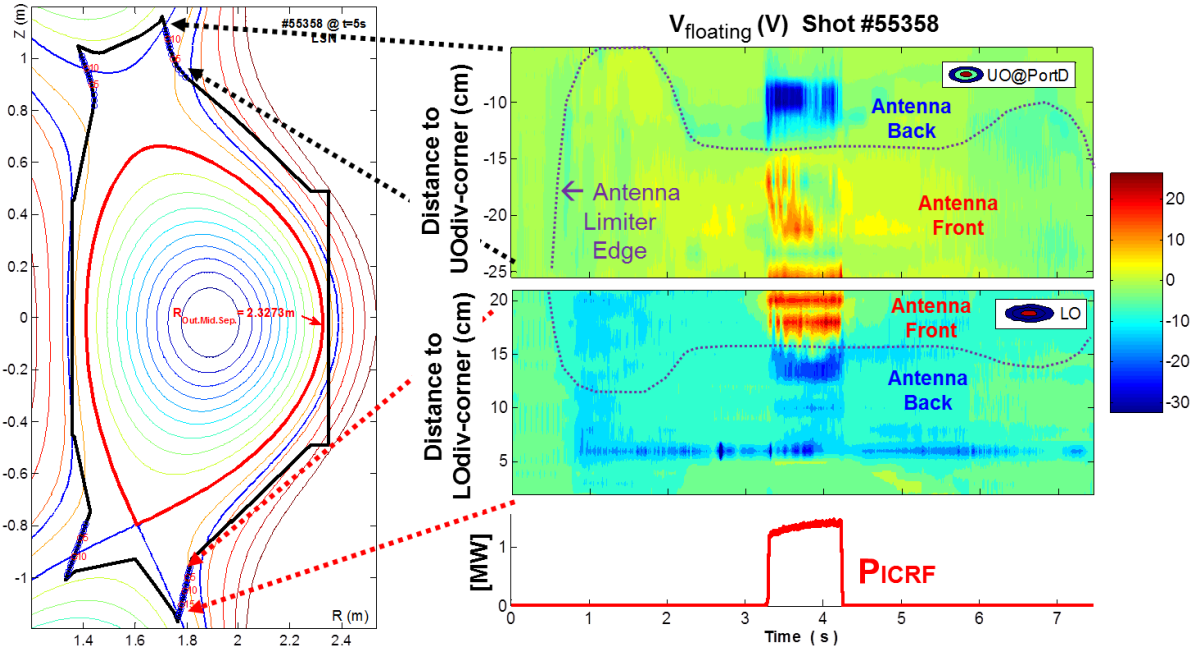
Figure 11. Time evolution of Langmuir probes floating potential V_f profiles of both upper and lower divertors outer targets during a LSN discharge. Regions magnetically connected to the front and the back of the antenna limiter edge are separated by the dotted purple curve.
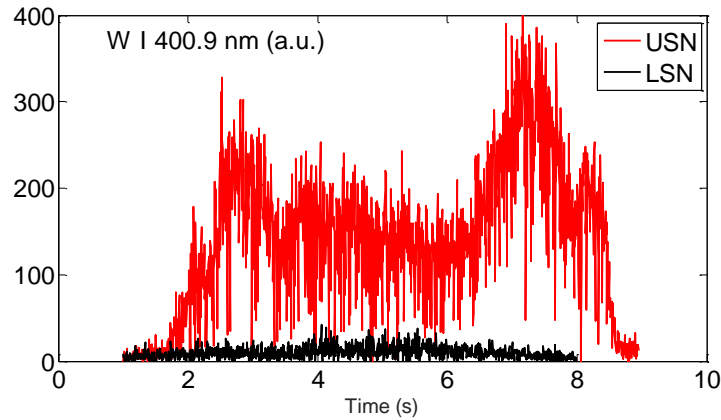
Figure 12. Time evolution of W^+ emission (at 400.9nm) measured by visible spectrometer at upper outer divertor target in both LSN (#55358) and USN (#69671) magnetic configurations

3.3 Near-field effects on main chamber objects magnetically connected to active antennas

Surfaces close and magnetically connected to active ICRH antennas are often subject to much stronger interactions with plasma due to RF sheath excitation. When the incidence angle of the connection is high (almost normal), effects can be particularly deleterious as shown in this section. Figure 13 represents Ti (magnetically connected to B-port) and Fe (present in antennas Faraday screens) as functions of both P_{ICRH} and P_{TOT} such as in Figure 8.

As expected from Figure 3a and Figure 3b, magnetically connected species are well correlated to P_{ICRH}. Figure 13a shows that Ti is very sensitive to discharge conditions as each series behaves differently, whereas Fe has different behaviours but globally increases with P_{ICRH} (Figure 13b). At constant LH power and same ICRH power on each strap (blue series), Ti and Fe both follow linearly P_{ICRH}. For constant ICRH power, we observe much higher Ti content when the power is unbalanced (red series) than when it is well balanced (blue series). When ICRH increases together with LH power (black series), Ti remains constant, showing that interactions in regions closely connected to the B-port antenna may not only depend on ICRH

power but also on how it is launched (antenna design, power balance on straps). Fe from antenna Faraday screens always increases with ICRH power in a similar fashion in all cases showing a generally good correlation. Fe sensitivity to one single antenna's settings is however less obvious than for Ti since Fe can come from both antenna Faraday screens.

In Figure 13c and Figure 13d representing Ti and Fe increase as function of P_{TOT} a group of red dots corresponding to the red series in Figure 3a and Figure 3b with unbalanced power on straps, is significantly above the others, whereas these cases are not different than others from the divertor's perspective (Figure 8b). For magnetically connected species, in the absence of ICRH, the impurity concentration seems independent of the LH power, at least in the 1-2.5MW power range. This confirms Ti and Fe closely connected to antennas are mostly sensitive to ICRH settings and near-field effects.
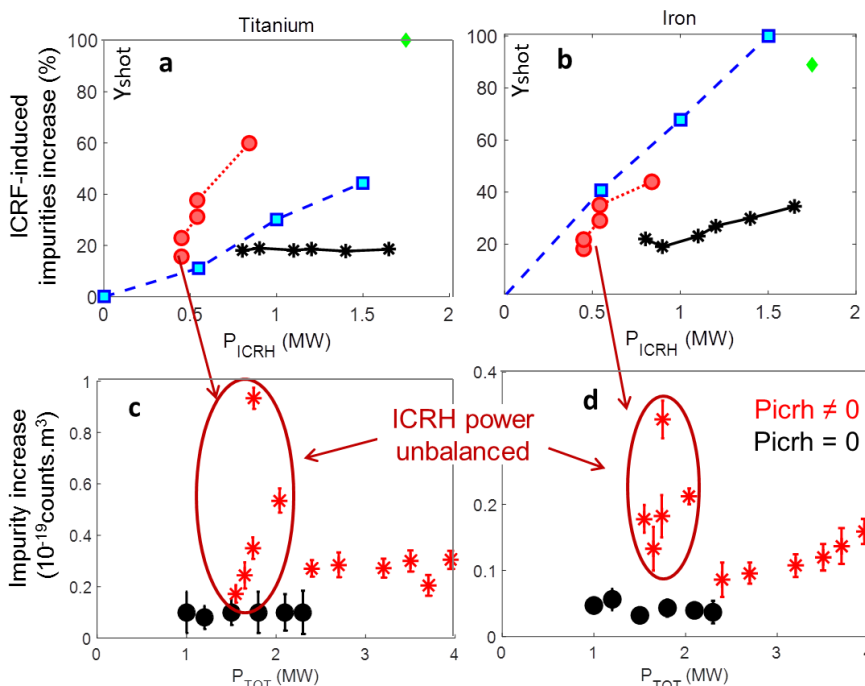
Figure 13. Ti and Fe production (Y_{shot}) as a function of (a & b) ICRH power and (c & d) total power. Blue, red and black series in graph a correspond to the same shots as in Figure 7. Graph b also represents to the same shots but points without ICRH (black series) were added as well.

Following similar philosophy as for the Ti plate near E-port, two other stainless steel plates were coated with a 5μm layer of Ag (silver) and fixed in 2018 on one limiter of the I-port antenna (the one on the H-port side). This region was chosen as it is very well connected to the I-port and pretty much nothing else. The limiter between G and H ports being radially 1cm closer to the plasma than the antenna limiters, no fast electron accelerated by the LH launcher in E-port can either reach this region. The idea of using Ag as an impurity trace of plasma surface interactions resulting from I-port near-field effects did not work out since no line corresponding to Ag was found in the spectra. However, the plates melted at each corner over about 4cm poloidally, precisely where HFSS model predicts peaks of RF potential due to sheath excitation [20]. As furthermore shown in Figure 14, the part that melted on each plate (represented by the stars) is distinct from the one that was the closest to the plasma (represented by the circles). This is therefore an example of the consequences near-fields excited RF sheath may have on plasma surface interactions.

Knowing all the characteristics of the plate and that stainless steel would start melting between 1300 and 1400°C, a thermal analysis made with ANSYS – which details are given in Appendix – provides an estimation of the minimal heat flux that may have induced plates melting. Assuming the heat fluxes were mostly parallel, a parallel flux above 5MW/m² would suffice to induce partial melting of the plate in less than a second. Identifying #78578 as one of the most likely shot of 2018 campaign during which such conditions might have been

reached (1.7MW on I-port with 60° phasing and power unbalanced on the straps), we can estimate SOL electron temperature ($T_e \approx 20eV$) and density ($n_e \approx 3.10^{17}m^{-3}$) with nearby Langmuir probes. Following the simplest models in the literature [37] and assuming that parallel heat fluxes are entirely due to DC potential drop across the sheath [38], it is finally possible to estimate the DC potentials that would have been necessary to reach such heat fluxes through the parametric scaling

$$V_{DCsheath} = \frac{Q_\parallel}{\Gamma_{Bohm} e} \approx \frac{Q_\parallel}{n_e \sqrt{T_e + T_i}} \approx \frac{Q_\parallel}{n_e \sqrt{3 T_e}} = 600V \qquad (4)$$

600V happens to be a value pretty consistent with typical potentials measured by Langmuir probes (several hundred volts) not specifically connected to the region of the maximum.
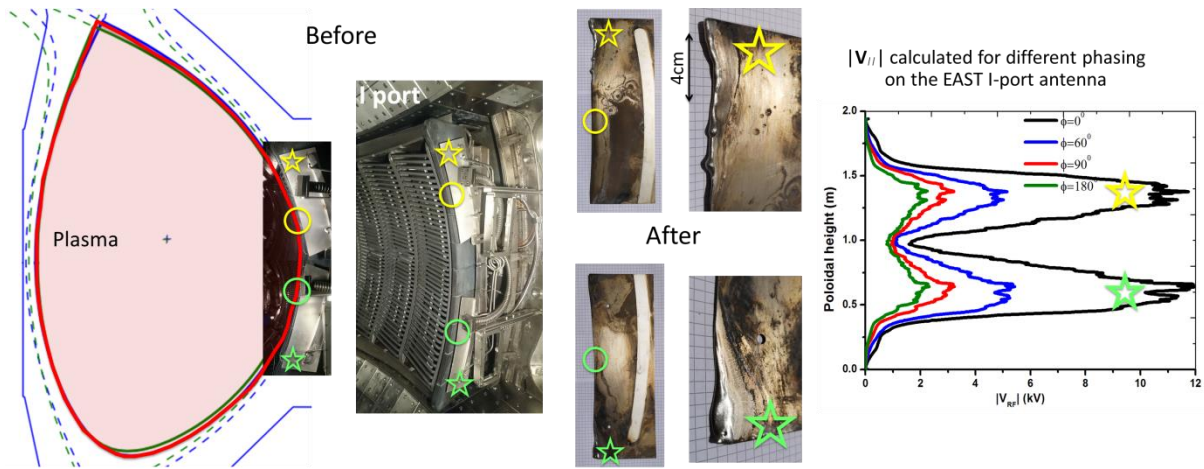

Figure 14. Pictures of the plates fixed on I-port antenna limiter, before and after 2018 campaign. Green and yellow circles represent respectively the part of the lower and upper plate that is the closest radially, while the stars represent the region that melted. The graph to the right shows that maximum of sheath potential computed with HFSS are precisely expected in the region where plates melted. On pictures taken after the experiment, plates are superposed on a grill of 5mm squares to give an idea of the dimensions.

In order to better represent the impurity correlation with P_{ICRH}, we focus on the black series based on maximum number of points and for which each species shows significantly different behaviours. For those shots, ICRH-related impurity production is now represented relatively to the species with the highest ratio P – representative of how likely a given species is to contaminate core plasma when turning ICRH on – which happens to be Fe amongst Ti and W (Figure 15).

$$P = (Imp_{withIC} - Imp_{withoutIC}) / \mathrm{m}ean(Imp_{withIC} - Imp_{withoutIC})_{over.black.shots} \qquad (5)$$

The indicator of correlation is now noted $Y_{species}$ and is calculated as

$$Y_{species} = (Imp_{withIC} - Imp_{withoutIC}) / \max(P)_{over.all.species.and.shots} \qquad (6)$$

Error bars correspond to the root mean square of $Y_{species}$ for the time periods during which Imp_s are assessed. This quantity is basically representative of each species' correlation with P_{ICRH}. Figure 15 typically shows that Fe is the species that best correlates with P_{ICRH} which is consistent with the fact that it mostly comes from antenna Faraday screens where the strongest near-fields are expected. Ti farther away from antennas and magnetically connected to the B-port undeniably depends on P_{ICRH}, but mechanisms other than just RF sheath excitation seem to play a role, as simply increasing P_{ICRH} does not necessarily enhance Ti production. W, an element that used to be found only in components in the divertor region, appeared weakly correlated to ICRH power compared to Fe. But this situation changed in 2018 when both LH

launchers guard limiters were changed into tungsten (Figure 1). Comparing both situations now allows in the last section to quantify these limiters contribution to core W content.
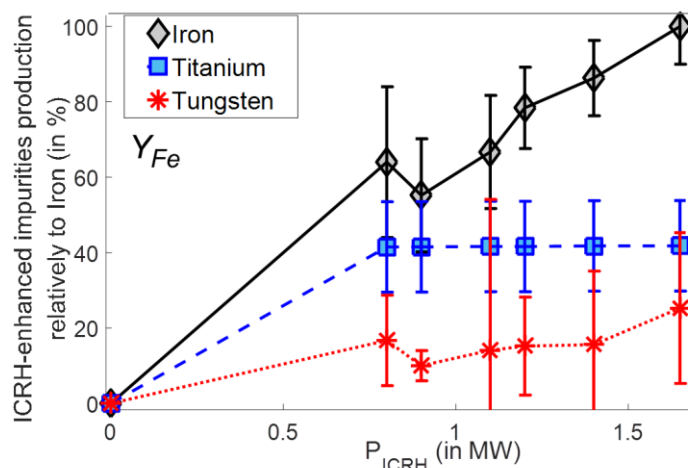
Figure 15. ICRH impurities production increase relatively to Fe (Y_{Fe}) as a function of ICRH power

4. Quantify the contribution of LH grill limiters to core W contamination in EAST from LSN/USN comparisons.

In 2018, one of the main upgrades made in EAST concerned both LH launchers' lateral protections which used to be composed of graphite tiles and were fully replaced by tungsten tiles with different designs on each grill (Figure 16b). Like in other devices like ASDEX Upgrade [33], having W at the mid-plane substantially changes the impurity production picture we got in the previous sections, and this will now be compared to complement the discussion before concluding. As shown in Figure 12 by visible spectroscopy data providing a rather direct estimation of W emission at the divertor, much stronger erosion occurs in USN rather than LSN. This is consistent with core W content whose ratio in USN against LSN are plotted in Figure 16a. The black dotted curve represents the core W content ratio between similar discharges in USN versus LSN when W was still characteristic of divertor region, typically showing that erosion rate in USN was about 8 times higher than in LSN. The red solid curve represents the same quantity after the 2018 upgrade for discharges without ICRH (#77724 over #77722). Having W at the mid-plane led to homogenization of W core contents in different configurations, suggesting that the contamination efficiency by divertor sources is negligible compared to mid-plane one.
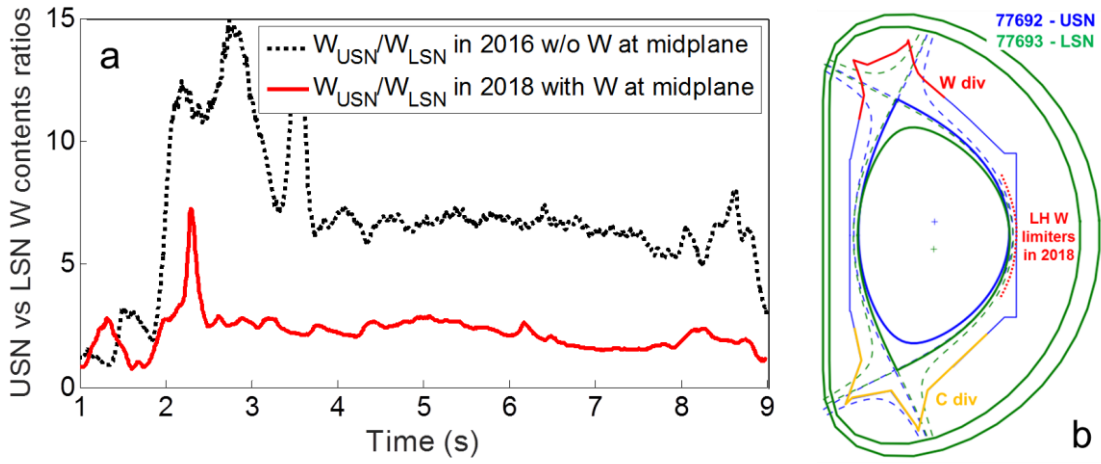
Figure 16. (a) Comparison of W contents ratios between similar shots without ICRH in USN and LSN configurations, with (2018 red solid curve) and without (2016 black dashed curve) W present at mid-plane. (b) USN vs LSN EFIT magnetic equilibriums

In order to quantify the contribution of LH limiters to core contamination by W, we will make the following assumptions:

- A1) The core W content on EAST can be decomposed into 3 contributions:
  - W1 from W upper divertor
  - W2 from LH limiters
  - W2 from LH limiters
  - W3 from "elsewhere" in the main chamber (unknown…)

With these notations, we basically want to estimate the relative contribution of LH limiters to the core contamination, *i.e.* the ratio W2/(W1+W2+W3).

- A2) W2=0 before the tungstenisation of LH limiters.
- A3) W2 and W3 remain the same in USN and LSN configurations.
- A4) W1=0 in LSN configuration.
- A5) W3/W1 is the same before and after tungstenisation of LH limiters.

Assumptions A3 and A4 are used to discriminate the location of the sources. They imply that there is no W source (*e.g.* specific from the lower divertor) that would appear only in LSN configuration. A2 is necessary to discriminate LH limiter contribution from the rest. A5 means that LH limiters tungstenization is the main change in the machine, ideally the only one. Under the above assumptions USN *vs*omparison before tungstenization of the LH limiters estimates W3/W1:

$$\left(\frac{LSN}{USN}\right)_{before} = \frac{1}{1 + W1/W3} \tag{7}$$

USN *vs* LSN comparison after tungstenization estimates (W3+W2)/W1.

$$\left(\frac{LSN}{USN}\right)_{after} = \frac{1}{1 + W1/(W2 + W3)} \tag{8}$$

Whence the estimated ratio W2/(W1+W2+W3) without ICRH leads to

$$\frac{W2}{W1 + W2 + W3} = \frac{\left(\dfrac{LSN}{USN}\right)_{after} - \left(\dfrac{LSN}{USN}\right)_{before}}{1 - \left(\dfrac{LSN}{USN}\right)_{before}} = \frac{\dfrac{1}{3} - \dfrac{1}{8}}{1 - \dfrac{1}{8}} = 25\% \tag{9}$$

In presence of ICRH however, one can expect much higher values [?]. Unfortunately this could not be done in EAST because the lower divertor was not used at all during most recent experiments campaign.

Note the actual ratio probably depends on the level of ICRH power compared to the total additional power, on the fraction of ICRH power emitted by each ICRF antenna, on the strap phasing, Li conditioning …
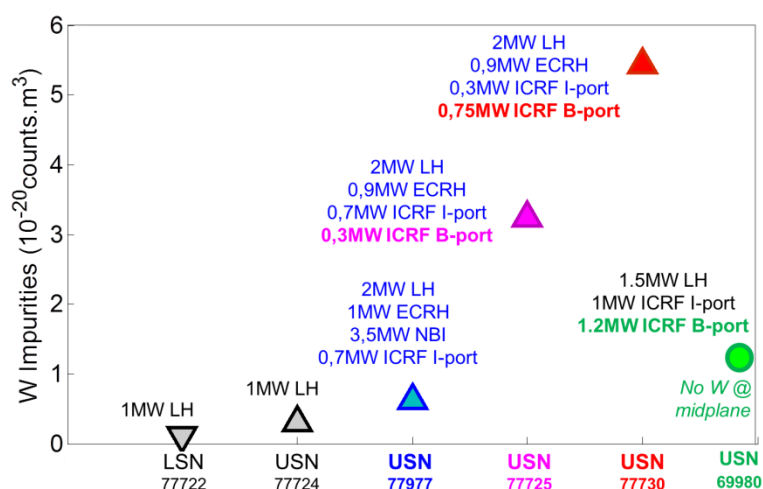
Figure 17. With W present at mid-plane, comparison of W contents in one LSN and four USN discharges with different heating scenarios. The large difference when B-port ICRH antenna is powered suggests that main sources are magnetically connected LH launchers limiters.

W content in the core for the two same discharges heated with 1MW LH power during the 2018 campaign were represented by black triangles in Figure 17. The small difference between these similar discharges in different configuration ($W_{USN} < 2.W_{LSN}$) suggests principal W sources are now located at mid-plane. Other USN discharges with different heating scenarios were displayed on the same graph. The blue triangle stands for a discharge heated with all heating systems except the B-port ICRH antenna and we see, despite the relatively high amount of power injected (7.2MW in total with about half from NBI), that the W level remained relatively low. In another shot however (magenta triangle), the 3.5MW from NBI were replaced by 0.3MW ICRH from B-port, and the W content rose more than fivefold. Finally, another discharge followed with similar total power injected but having 350kW ICRH injected from the B-port rather than from the I-port (red triangle), which led to another sharp increase of the W content. These results are consistent with magnetic connections existing between ICRH antennas and LH launchers limiters. As can be seen on Figure 1, the I-port antenna only connects to the upper part of the N-port LH grill and does not connect to the E-port grill shadowed by the limiter between the G and H ports. The B-port antenna is however well-connected to both LH launchers, therefore enhancing interactions with W limiters. These results together show that W sources in a mid-plane region magnetically connected to an active ICRH antenna can lead to severe core contamination by W. To put it differently, this experiment proves that the ICRH antennas should have no magnetic connection with a normal incidence to objects into the vacuum chamber.

4 Discussions and prospects

By using the EUV spectrometer to characterize the presence of high-Z metallic impurities in the core, and benefiting from the multiplicity of materials in EAST, we were able to deduce local information about ICRH-related plasma surface interactions.

Magnetic connection between objects of specific composition and active antennas undeniably plays a role which becomes more and more complex as the distance to active antennas increases. Fe from antenna Faraday Screens typically correlates well with ICRH power, which is believed to be the result of near-field enhanced interactions, so far consistent with most observations elsewhere [3-10]. Rectification effects are then transported along magnetic field lines from active antenna to connected regions, as observed through the Ti content evolution when degrading the power balance on antenna straps. This observation is consistent with uncompensated image currents induced on antenna limiters, leading to stronger potential rectification at the Ti plates [9]. Besides, for well-balanced power on straps, ICRH-induced rectification can be inhibited in the same region. This could additionally be the result of improved wave absorption by increasing total injected power which would require a dedicated study including more precise calculations of wave absorption efficiency. When W was still exclusive to the upper divertor region, it used to show much better correlation with total conducted power rather than with ICRH power, or settings like power balance or phasing between straps. Divertor outer target was identified in others devices to be an important source of impurities [13, 14, 24] but not specifically due to ICRH [12, 15]. In EAST, potential rectifications are observed by divertor Langmuir probes [25]. These increase together with ICRH power and occur in comparable fashion either in LSN or USN. On the contrary, erosion rates are very different and depend on magnetic configuration, which leads to the belief that, unlike observation from other experiments [30, 34], the poor level of ICRH power injected in EAST may not suffice in the divertor region to rectify the sheath up to the critical regime of sputtering (Fig. 1 in [25]). At the mid-plane, on the contrary, the connection length to the ICRH antennas and the SOL width being much shorter than in the divertor region, both RF-induced erosion rate [15] and impurities penetration [13] are higher. Therefore changing lateral protections of the two LH launchers from graphite into W, leads to comparable core contamination by W in different magnetic configurations, meaning dominant impurity sources are located at mid-plane. Moreover, mid-plane erosion of W is particularly strong when connected ICRH antenna is powered. As far as EAST L-mode plasmas are concerned, we therefore conclude that RF sheath is the mechanism that widely dominates plasma materials interactions and core contamination by impurities. We even collected evidence of metallic plates melting induced by RF sheath excitation on antenna corners, which also motivates further study based on camera images to extract information on how impurity penetrate inside the plasma.

Most metallic impurities were moreover insensitive to ICRH phasing that was not feedback controlled [26], which is not consistent with similar experiments and modeling predictions [1, 9, 24] as shown in appendix 2. Only Mo reacted to phase changes with increasing interactions over phase scan from dipole to monopole. If Mo were to come from low field side due to near fields, Fe should have similar behavior, which was not the case. We therefore believe Mo comes from the part of the high field wall facing I-port antenna. This hypothesis is consistent with wave propagation and absorption modeling with EVE [27] and TOMCAT codes [28]. As phasing decreases from dipole to monopole; (i) single pass absorption efficiency shrinks from 55% down to 15%, (ii) low $k_{//}$ modes are excited for phasing bellow 60° ($\sim k_{//} < 3m^{-1}$), and (iii) electric field amplitude increase at the high field side, likely enhancing plasma surface interactions on Mo target.

Experimentally, difficulties still arise on a poor estimation of the ICRH power injected in the vessel as losses in transmission lines should not be neglected. It should be pointed out

that the two ICRH antennas have different designs and sizes, meaning that not only the magnetic connection but also the antenna design can both play a role in impurity generation [9]. Note that the B-port is systematically the principal cause of impurity production up to deleterious levels, which can be partially understood considering its smaller size compared to the I-port, leading to higher power density for similar generator power and loading [20].

Appendix

A1) Complements on EVE and TOMCAT modelling of ICRH wave propagation and absorption in EAST

In order to better enlighten wave properties in EAST, Fig.A1 represents fields polarization in different regions and for different phasing computed by EVE [27] showing mode conversion and increasing fields amplitudes at the high field side as phasing decreases down to monopole.
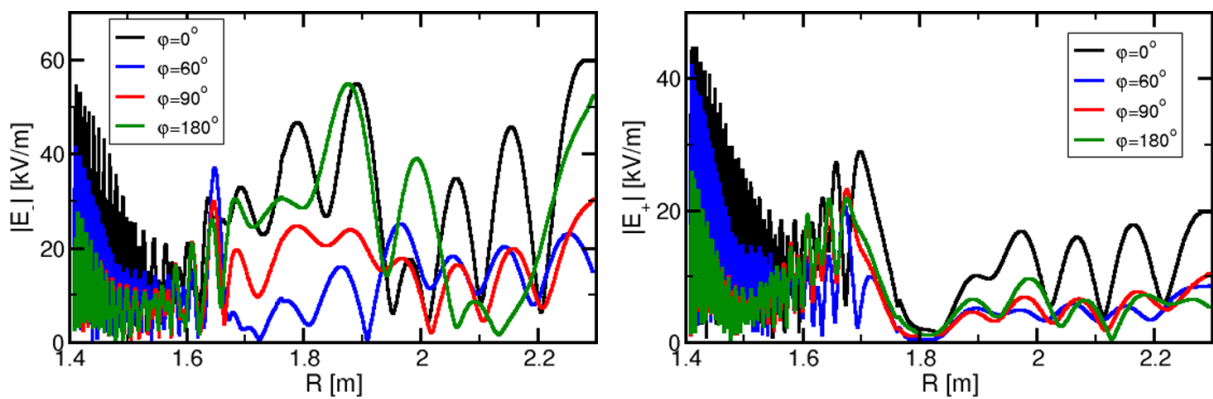
Figure A1. Radial evolution of the amplitudes of the negative (left) and positive (right) polarizations of the electric field (from low field side to the right up to high field side to the left)
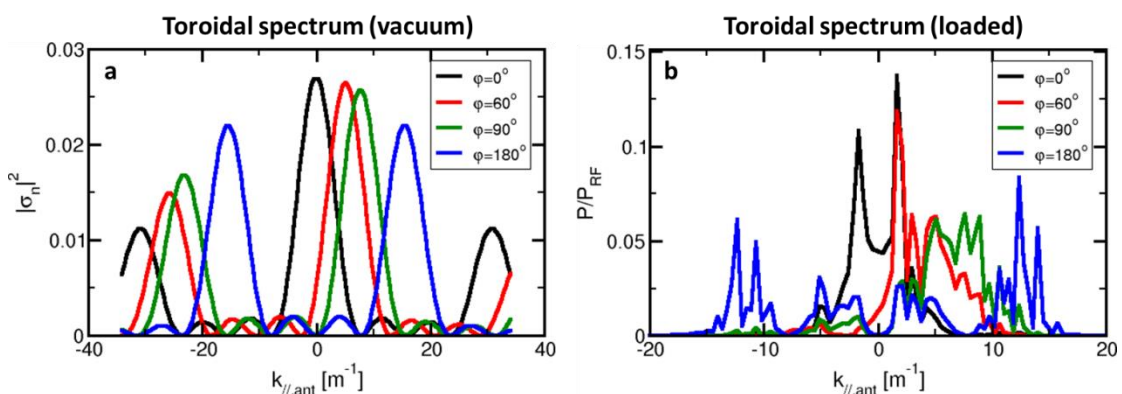
Figure A2. Antenna toroidal spectrums for different strap phasing (0°, 60°, 90°, 180°), (a) in vacuum and (b) in front of EAST plasma load (reference shot 69950).

Fig.A2 also shows $k_\parallel$ spectra in vacuum and loaded by EAST plasma. It can be clearly seen on the loaded spectrum that a low $k_\parallel$ mode is excited bellow 60° phasing. Low $k_\parallel$ mode absorption might be poor, potentially leading to proper modes in the plasma and power dissipation into the SOL with deleterious impact on plasma surface interaction.

A2) V_{DC} evolution over phase scan – SSWICH model

In view of providing an idea about how potentials induced around the antenna structure vary over a phasing scan, DC rectified potentials were computed for each phasing case of Fig.A4 with SSWICH-SW code [35], and 2D maps represented on Fig.A4 were extracted along the limiters' poloidal extent and over a 6cm radial range. Since no 3D model of the EAST I-port antenna exists, calculations were done based on the JET-A2 antenna geometry which is very similar yet about twice bigger as shown in Fig.A3. We acknowledge the different aspect ratio of both antennas that prevents from extrapolating quantitative results with one antenna to the other, yet the qualitative changes along phase scan can be considered as fairly acceptable and common to a wide variety of ICRH antennas.

Fig.A4 shows how DC potential induced in front of an antenna limiter increases over a phase scan going from dipole to monopole. This can be understood thinking in terms of proximity effect [36] and compensation of currents induced on limiters [9]. In the dipole case (180° phasing), currents from adjacent straps both induce currents in opposite directions on limiters which tend to compensate each other. However on the monopole case (0° phasing), current on all straps are in the same direction such that they all contribute to increase induced-currents, therefore leading to stronger potential rectification and impurity production.
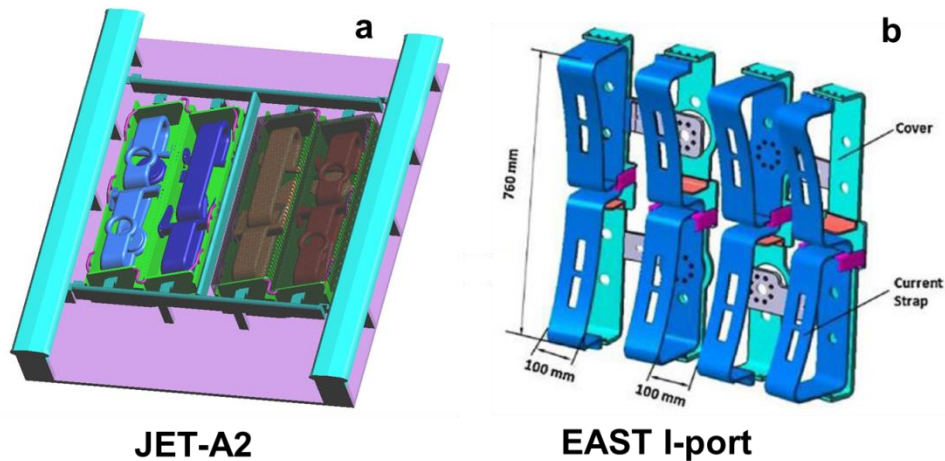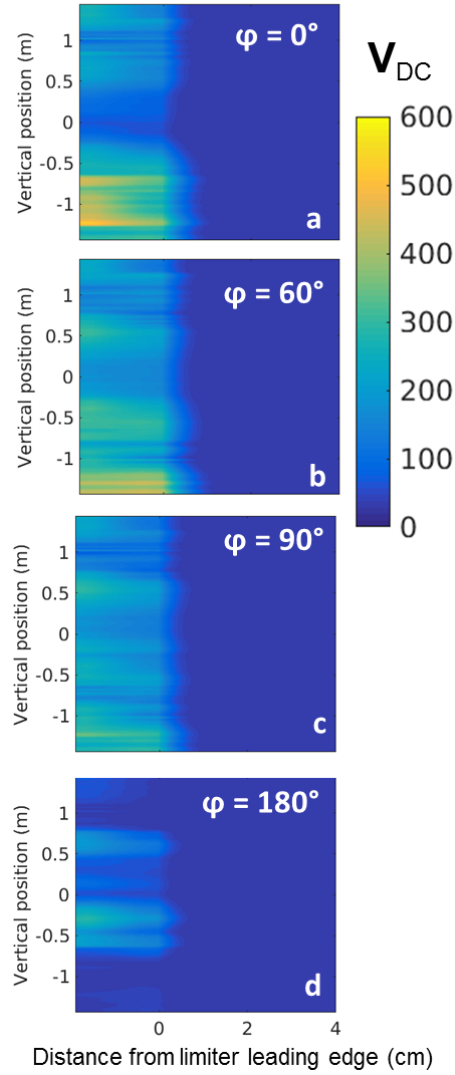

Figure. A3. Similar 3D geometries of (a) JET-A2 and (b) EAST I-port antennas

Figure A4. DC rectified potentials were computed along limiter poloidal height and over a 6cm radial range with SSWICH code [35] for each phasing case of Fig. 4, namely (a) monopole (0, 0, 0, 0), (b) (0, π/3, 2π/3, π), (a) current drive (0, π/2, π, 3π/2) and (d) dipole (0, π, 0, π)

A3) ANSYS estimation of RF-sheath induced heat fluxes on I-port antenna corners necessary to induce metallic plates melting

In this simulation with ANSYS, we consider an inertial stainless steel plate of 30cm (poloidally) x 10cm (radially) x 1mm (toroidally).The heat flux is assumed parallel (toroidal) and its maximum is found at the closest edge to the plasma, 3cm away from a corner of the plate (Fig. A5). From this maximum, heat fluxes decrease exponentially in both radial and poloidal directions, as per focusing mostly on RF sheath induced heat flux.

Dynamic simulations where made for five different values of maximal heat flux from 1 to 10MW/m², and plate maximal temperature evolution represented in Fig. A6. Note values estimated in Tore Supra and JET would typically be of the order of 2 to 7MW/m² [38]. In EAST, these simulations predict that plate would have started melting after 30s for a maximal heat flux of 3MW/m², after 15s for 5MW/m², and only after 2s for maximal heat flux of 7MW/m².
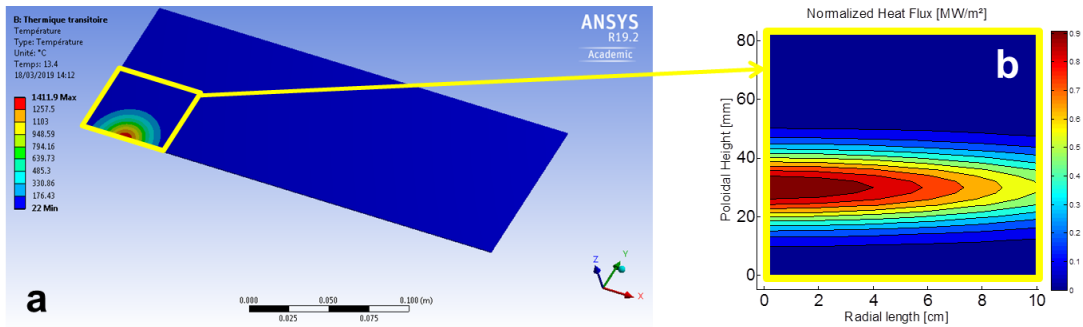
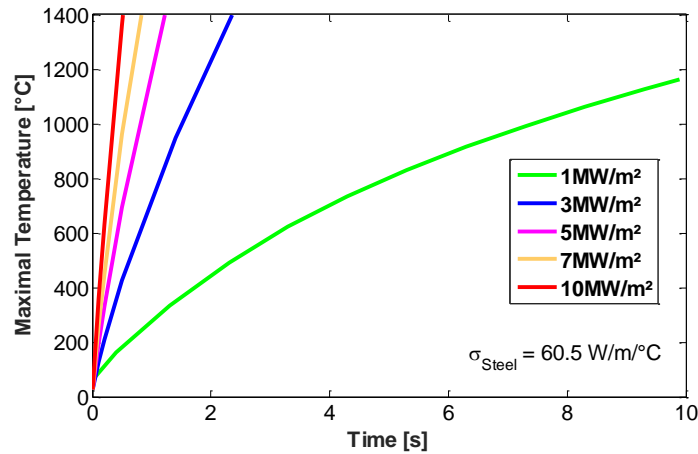Figure. A5. (a) ANSYS model with (b) heat loads pattern on the metallic plate corner

Figure A6. Evolution of the maximal temperature of the plate for different parallel heat fluxes calculated with ANSYS. Steel plate starts melting when its temperature approaches 1400°C.

A4) Comparison of surface temperature estimations from infrared and temperature inversion with TEDDY code on EAST I-port graphite limiter tile

Despite no infrared camera was looking at the metallic plates shown in Fig. 14, a camera was fixed and added in K-port in 2019, allowing good resolution infrared measurements on the I-port antenna (Fig.A7). During discharge 83746 made in 2019, the power was far from balanced on the straps with power changing between 50kW up to 350kW from one strap to its neighbour. Already suspecting from past year that the plate most likely melted due to this type of setting unfavourable for RF sheath excitation, we analysed the apparent temperature on the antenna bottom corner symmetric to where the plate melted. The temperature remained fairly low along the discharge and saturated at about 300°C in about 20ms as the antenna was powered. Visible on the video, spectacular graphite dusts were also emitted from the hot spot with surprisingly deep penetration before getting ionized and starting following magnetic flux tubes. This peculiar observation is not yet understood and will be the object of future investigation. In order to get an estimation of which heat flux would have been necessary to induce such apparent temperature increase on the infrared camera, we used TEDDY code [39] recently developed in CEA which is inspired of THEODOR [40] and basically takes into account further non-linear processes. By prescribing a 10MW heat flux on the target with similar pattern as the one shown in Fig.A5b, we see that we recover the same temperature increase as the one observed by the IR camera. Note finally this heat flux is twice larger than the one that would have been necessary to melt the plates based on ANSYS estimations.
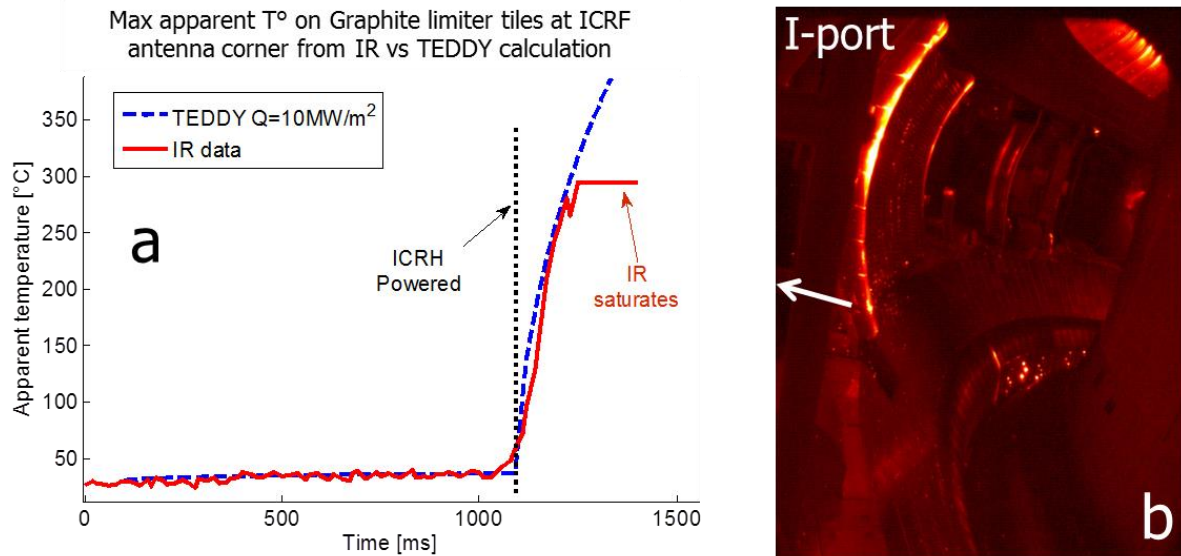
Figure. A7. EAST I-port ICRF graphite limiter corner maximal apparent temperature estimation from infrared camera (red curve) superposed onto temperature increase induced by 10MW/m² heat fluxes and estimated with TEDDY code.

References

[1] J.H. Zhang et al. Nucl. Fusion 57 (2017) 066030 (10pp)
[2] G. Urbanczyk et al EPJ Web of Conferences 157, 03057 (2017)
[3] L Colas et al. Plasma Phys. Control. Fusion 49 (2007) B35–B45
[4] M. Kubic et al. Journal of Nuclear Materials 438 (2013) S509–S512
[5] R Ochoukov et al Plasma Phys. Control. Fusion 56 (2014) 015004
[6] I. Cziegler et al, Plasma Phys. Control. Fusion 54 (2012) 105019
[7] R. Hong et al. Plasma Phys. Control. Fusion 59 (2017) 105008
[8] V. Bobkov et al. Journal of Nuclear Materials 438 (2013) S160–S165
[9] V. Bobkov et al. Plasma Phys. Control. Fusion 59 (2017) 014022
[10] M.J. Martin et al. PRL 119, 205002 (2017)
[11] Y Q Yang et al. Plasma Phys. Control. Fusion 59 (2017) 095001
[12] R. Dux Journal of Nuclear Materials 390–391 (2009) 858
[13] B. Lipschultz, D.A. Pappas, B. LaBombard et al, Nucl. Fusion 41, p.585 2001
[14] S. Wukitch et al Journal of Nuclear Materials 390–391 (2009) 951–954
[15] R. Dux et al. Journal of Nuclear Materials 363–365 (2007) 112–116
[16] L. Zhang et al 2015 Rev Science Instruments, 123509
[17] Z. Xu et al 2018 Nucl. Fusion 58 016001
[18] H. Mao et al. Nuclear Materials and Energy 12 (2017) 447–452
[19] M. H. Li et al. Physics of Plasmas 23, 102512 (2016)
[20] Qin Chengming et al. Plasma Science and Technology, Vol.17, No.2, Feb. 2015
[21] Zhang et al. Rev. Sci. Instrum. 86, 123509 (2015)
[22] S. Wukitch et al APS Division of Plasma Physics Meeting 2014 DPPUO3012W
[23] V. Bobkov et al, Nuclear Materials and Energy 12 (2017) 1194–1198
[24] K. K. Kirov - Plasma Phys. Control. Fusion 51 (2009) 04400
[25] E. Lerche et al AIP Conference Proceedings 1187, 93 (2009)
[26] Chen Z, Zhao YP, Chen G. et al. NUCL SCI TECH (2018) 29 19
[27] R. Dumont, Nuclear Fusion 49, 075033 (2009)
[28] D. Van Eester and E. Lerche. Plasma Phys. Control. Fusion 55 (2013) 055008
[29] E. Lerche et al. Plasma Phys. Control. Fusion 50 (2008) 035003
[30] J.C. Xu et al, Review of Scientific Instruments 87, 083504 (2016)
[31] R. Perkins et al EPJ Web of Conferences 157, 03039 (2017)
[32] R. Perkins et al Physical Review Letters 109(4) · July 2012
[33] V. Bobkov et al. 2010 Nucl. Fusion 50 035004
[34] R J Perkins et al 2019 Plasma Phys. Control. Fusion 61 045011
[35] J. Jacquot et al, Phys. Plasmas 21 061509 (2014)
[36] L Colas et al. Plasma Phys. Control. Fusion 59 (2017) 025014
[37] Perkins F.W., Nuclear Fusion 29 (4) 1989, p. 583
[38] L Colas et al. RFPPC 2009
[39] N. Fedorczak et al. PFMC 2019 "Infra-red thermography estimation of deposited heat load dynamics on the lower tungsten divertor of WEST"
[40] A. Hermann et al, Plasma Phys. Control. Fusion 37 (1995) 17.